PCCP

PAPER

View Article Online
View Journal | View Issue

Cite this: *Phys. Chem. Chem. Phys.*, 2019, **21**, 12372

Critical fracture properties of puckered and buckled arsenenes by molecular dynamics simulations

Bo Yang,[a] Maodong Li,*[a] Jiye Wang,[b] Jingchao Zhang,[c] Dongmei Liao[d] and Yanan Yue *[d]

Received 21st March 2019,
Accepted 13th May 2019

DOI: 10.1039/c9cp01605h

rsc.li/pccp

The pioneering prediction and successful synthesis of monolayer arsenene in recent years have promoted intensive studies on this novel two-dimensional (2D) material. Strain-engineered arsenene monolayer can change its geometric structures with tuned charge distribution, which paves the way for achieving novel electronic properties. The practical applications of the strain-driven topological state in arsenene strongly depend on its critical strain value. In this work, mechanical properties such as fracture strain, fracture strength and Young's modulus of two arsenene structures, *i.e.* buckled arsenene (b-arsenene) and puckered arsenene (p-arsenene), are comprehensively investigated under different modulators such as system dimension, chirality, temperature, strain rate and random surface defect. A maximum fracture strain reduction of 41.7% from 0.24 to 0.14 is observed in armchair b-arsenene when the temperature increases from 100 to 500 K. The most significant impact factor on the mechanical properties of arseneneis found to be surface defects. A maximum fracture strength reduction of 85.7% is predicted in the armchair b-arsenene when the defect ratio increases from 0 to 5%. On the other hand, the strain rate has a negligible effect on the mechanical properties. Our results provide fundamental knowledge on the critical fracture properties of arsenene.

1. Introduction

Young's modulus of a monolayer graphene sheet was measured to be 1.0 TPa, which established graphene as an extremely high stiffness material.[1] Due to its unique two-dimensional (2D) structure, graphene possesses extraordinary thermal, optical and mechanical properties. The emergence of graphene has attracted numerous research efforts both experimentally and numerically.[2–6] However, the lack of a bandgap hinders its applications in semiconductor devices. One of today's most challenging material science problems is the development of thermoelectric materials with high figure of merit $ZT = \sigma S^2 T/(\kappa_e + \kappa_l)$, where S is the Seebeck coefficient measuring the magnitude of an induced thermoelectric voltage at a given temperature T, σ is the electrical conductivity and κ_e and κ_l represent electronic and lattice thermal conductivities, respectively. Recently, monolayer arsenene composed of arsenic (As) atoms has been proposed as a promising thermoelectric material with high ZT.[7] The buckled arsenene monolayer exhibits a larger ZT value than phosphorene, which is 0.17 at 700 K.[8] Upon doping, the buckled arsenene monolayer could become a competitor of well-established thermoelectric materials (ZT = 0.8). The n-type doped arsenene monolayer possesses superior thermoelectric properties relative to the p-type doped arsenene monolayer.[9] With multilayer arsenene nanoribbons being successfully synthesized on an InAs substrate using a plasma-assisted approach,[10] investigations of this new 2D material will attract growing attention in the near future. It has been found that the synthesized multilayer arsenene was not continuous, implying that it was like a pile of multilayer nanoribbons. Its thickness could be changed by controlling the plasma exposure time.

It has been proved that both the buckled and puckered honeycomb structures of arsenene are stable.[11] The monolayer structures are predicted to be semiconducting which is different from its few layer structures.[12] An intriguing transition from the indirect-gap to direct-gap semiconductor at an in-plane biaxial strain of 4% and a uniaxial tensile strain of 1% has been reported in monolayer arsenene.[13] While in-plane strains can directly change the lattice constants and other geometric parameters, the cross-plane vertical strain modulates the buckling

[a] National Graphene Center (Guangdong), Guangzhou Special Pressure Equipment Inspection and Research Institute, Guangzhou, Guangdong, 510663, China. E-mail: 272818102@qq.com
[b] Weichai Heavy Machinery Co., Weifang, Shandong, 261108, China
[c] Holland Computing Center, University of Nebraska-Lincoln, Lincoln, NE 68588, USA
[d] Key Laboratory of Hydraulic Machinery Transients (MOE), School of Power and Mechanical Engineering, Wuhan University, Wuhan, Hubei, 430072, China. E-mail: yyue@whu.edu.cn

heights of layered arsenene. Under cross-plane compressive strains, the monolayer arsenene experienced a transition from an indirect-gap semiconductor to a metal.[14] The band gap of both puckered and buckled arsenenes can be tuned by applying strain. An indirect-to-direct gap transition occurs by applying strain.[13] Specifically, 1% strain is enough to transform puckered arsenene into a direct-gap semiconductor. It is remarkable that the system remains a direct-gap semiconductor for a wide range of strain values from −10% to 10% except in the vicinity of no strain. This is a significantly important result from an application point of view since it can accommodate possible structural deformations, which may arise during growth or device manufacturing, while retaining its direct-gap semiconducting behavior. The indirect-to-direct band gap transition found in puckered arsenene may open up the possibility of using this two-dimensional system in several optoelectronic devices such as light-emitting diodes and solar cells. Using the first principles density functional theory (DFT) approach, Xie *et al.*[15] calculated the structural and electronic properties of the InSe/arsenene bilayer under uniaxial tensile strain and an external electric field. The bilayer structure can withstand a larger tensile than compression strain without compromising the structural integrity. The bandgap can also be manipulated by uniaxial strains. A direct–indirect bandgap transition is observed in the InSe/arsenene bilayer under tensile strain. Also using DFT calculations, it has been predicted that under 12% tensile strain the bandgap of arsenene is closed, and when the strain is greater than 12%, the s–p inversion takes place.[16,17]

The strain-engineered arsenene monolayer can change its geometric structures with tuned charge distribution, bond strength and electronic orbital hybridization, which paves the way for achieving the novel electronic properties of the monolayer arsenene.[18,19] Strain engineering can be experimentally achieved by a substrate lattice constant mismatch. Although the thermodynamic, electronic and optical properties of arsenene have been investigated in recent studies,[20–23] its mechanical properties have not been fully explored and remain an open topic. Therefore, a comprehensive investigation of its mechanical properties is urgently needed.

The effects of strain rate on the mechanical properties of two-dimensional (2D) materials have been extensively studied such as graphene,[24–27] silicene,[28] hexagonal boron nitride,[29] phosphorene[30] and MoS_2.[31,32] When a material is subjected to external dynamic loading, its mechanical behavior is likely to be influenced by the strain rate, which is the rate of change in strain (deformation) with respect to time. There is continual interest in the strain rate effect on the mechanical properties of materials as long as there is a need to understand the material's response during impact events. Strain rate not only affects the mechanical properties but also affects the fracture mechanism. It has been reported that the tensile yield strain of single-wall carbon nanotubes increases slightly when the strain rate increases.[33] A relationship between failure strength, strain and time to failure with the strain rate is established in graphene by MD simulations.[27] Yi *et al.*[26] also showed that the failure strength and strain of graphene with a grain-boundary increase slightly with increasing strain rate. To the best of our knowledge, no study has been carried out on the strain rate effect on the mechanical properties of buckled arsenene (b-arsenene) and puckered arsenene (p-arsenene). Therefore, in this work, we investigate the effects of strain rate on the mechanical behavior of arsenene. Other modulators such as system dimension, chirality, temperature and surface defect are also explored. Eight b-arsenene and p-arsenene models with different dimensions are constructed. Temperatures from 100 to 500 K are explored with the randomly surface defect ratios from 0 to 5%. The effects of strain rates are explored at 5 different values from 1 to 25×10^{-4} ps^{-1}. In the following sections, computational methods are first explained, followed by the mechanical property results under each modulator with the corresponding discussions. The main conclusions are summarized in the last section.

2. Computational model

All simulations in this work are performed using a Large-scale Atomic/Molecular Massively Parallel Simulator (LAMMPS).[34] The time step is set to 0.1 fs (1 fs = 10^{-15} s). Periodic boundary conditions are applied in all directions. A vacuum space of 50 Å was created in the out-of-plane z direction to avoid cross-boundary interactions. The Stillinger–Weber (SW) potential developed by Jiang *et al.*,[35] which has been validated based on the first-principles method, is used to model the interactions among As atoms. The same set of SW potentials have been successfully employed to study the mechanical properties of various 2D structures such as MoS_2,[36] $MoSe_2$,[37] WS_2[38] and borophene,[39] indicating the validity of the parameterizations. The motions of atoms in the system are described by

$$E = \sum_i \sum_{j>i} \phi_2(r_{ij}) + \sum_i \sum_{j\neq i} \sum_{k>j} \phi_3(r_{ij}, r_{ik}, \theta_{ijk}), \quad (1)$$

where ϕ_2 and ϕ_3 represent the two-body and three-body terms, respectively, and are expressed as

$$\phi_2(r_{ij}) = A_{ij}\varepsilon_{ij}\left[B_{ij}\left(\frac{\sigma_{ij}}{r_{ij}}\right)^{p_{ij}} - \left(\frac{\sigma_{ij}}{r_{ij}}\right)^{q_{ij}}\right]\exp\left(\frac{\sigma_{ij}}{r_{ij} - a_{ij}\sigma_{ij}}\right), \quad (2)$$

$$\phi_3(r_{ij}, r_{ik}, \theta_{ijk}) = \lambda_{ijk}\varepsilon_{ijk}\left[\cos\theta_{ijk} - \theta_{0ijk}\right]^2 \times \exp\left(\frac{\gamma_{ij}\sigma_{ij}}{r_{ij} - a_{ij}\sigma_{ij}}\right)\exp\left(\frac{\gamma_{ik}\sigma_{ik}}{r_{ik} - a_{ik}\sigma_{ik}}\right), \quad (3)$$

where A, B, λ, p, q and γ are parameters to identify a reasonable choice of ϕ_2 and ϕ_3; r_{ij} and r_{ik} represent the distances between i, j and i, k atoms. The exponential functions provide a smooth and rapid decay of the interaction potential to zero and retain the potential short range, which is important for efficient molecular dynamics (MD) calculations. Parameter θ is the angle between two neighbor bonds composed of three atoms i, j and k, and θ_0 stands for the equilibrium angle. Overall, the ϕ_2 term describes the pair-wise bond length variations and the ϕ_3 term characterizes the neighboring bond angle variations.

The initial b-arsenene and p-arsenene structures are first relaxed using the Polak–Ribiere conjugate gradient (CG) algorithm,

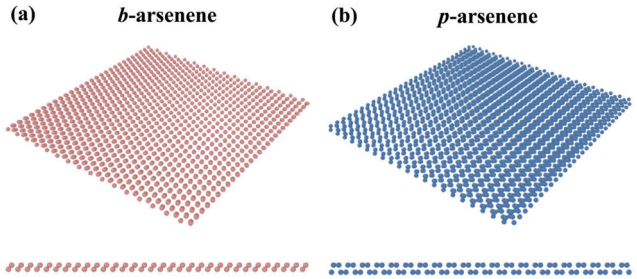

Fig. 1 Top and side views of (a) buckled arsenene (b-arsenene) and (b) puckered arsenene (p-arsenene).

where the force gradient is combined with the previous iteration information to compute the next search direction. After optimization, the structures are placed under an isothermal–isobaric (*NPT*) ensemble for 100 ps to reach a steady state. The elongation is performed at a designated strain rate under the *NPT* ensemble, in which the system elongation with time is given by

$$L_t = L_0(1 + \varepsilon \mathrm{d}t) \quad (4)$$

where L_t is the length of the system at time t, L_0 is the original system length and ε is the strain rate. Uniaxial displacement was applied on the boundary of the simulation box in either the armchair x or zigzag y direction, while maintaining the pressure on the other two directions as zero. Schematic plots of the atomic structures are shown in Fig. 1. The temperatures of 100, 200, 300, 400 and 500 K, and the strain rates of 1×10^{-4}, 2.5×10^{-4}, 5×10^{-4}, 1×10^{-3} and 2.5×10^{-3} ps^{-1} are used for each b-arsenene and p-arsenene sheets with or without defects. Random surface defects from 0 to 5% are created to investigate the effect of surface defect. The strain rates are selected to be small enough to allow the system to respond to the mechanical deformations, while being large enough for the simulation runs to be computationally feasible. For each case, we conduct five independent simulations under different initial conditions. The eventual values are averaged from five simulations with the standard deviations shown as error bars. For each MD simulation case, the fracture strain, fracture strength and Young's modulus are extracted from the strain–stress profiles.

3. Results and Discussion

To check the convergence of mechanical properties as a function of system dimensions, eight different models of b-arsenene and p-arsenene are constructed. Four b-arsenene models are created with dimensions of 0.9×1.0 $(x \times y)$ nm^2, 6.0×5.2 $(x \times y)$ nm^2, 9.8×9.9 $(x \times y)$ nm^2 and 24.8×21.5 $(x \times y)$ nm^2. The number of atoms for each system is 24, 600, 1792 and 9600, respectively. Another four different p-arsenene models are also created with dimensions of 0.8×0.9 $(x \times y)$ nm^2, 4.6×5.3 $(x \times y)$ nm^2, 9.8×10.1 $(x \times y)$ nm^2 and 18.9×21.9 $(x \times y)$ nm^2. The number of atoms for each system is 24, 600, 2352 and 9600, respectively. The reasons to investigate the effect of dimensions on the mechanical properties of b-arsenene and p-arsenene are two-fold. First, if the critical mechanical properties such fracture strain, fracture strength and Young's modulus do not change with the lateral dimensions of the system, smaller sizes are preferred considering the computational cost. For instance, when the system is 18.9×21.9 $(x \times y)$ nm^2, it took ~192 CPU hours to finish the computation. When the system sizes equal 0.8×0.9 $(x \times y)$ nm^2, the computation time reduces to 16 CPU hours. In this work, 6 different random defect ratios from 0 to 5%, 5 different strain rates from 1×10^{-4} to 2.5×10^{-3} ps^{-1}, and 5 different temperatures from 100 to 500 K are investigated. Each case is repeated 5 times to obtain the average value. Therefore, in total 80 different MD simulations are performed. By finding a smaller sized system, the computational cost can be significantly reduced. Second, in this work we investigated the effect of random surface defect on the critical mechanical properties of arsenene. To generate the evenly distributed random defects, the size of the system should be reasonably large. Considering the above reasons, moderate sized systems of 9.8×9.9 $(x \times y)$ nm^2 b-arsenene and 9.8×10.1 $(x \times y)$ nm^2 p-arsenene were selected for mechanical property predictions. The calculated fracture strain, fracture strength and Young's modulus variations with different system dimensions are shown in Fig. 2. The horizontal axis denotes the surfaces areas of different models. The mechanical properties are obtained at a temperature of 100 K and under a strain rate of 1×10^{-4} ps^{-1}. Based on the prediction results, it is observed that for both b-arsenene and p-arsenene, the fracture strain and strength first decrease with increasing

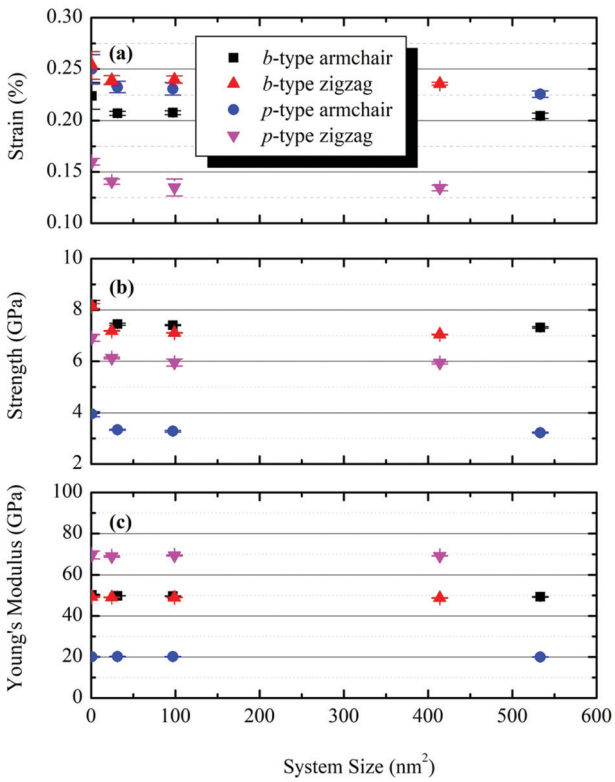

Fig. 2 Effects of system dimensions on the (a) fracture strain, (b) fracture strength and (c) Young's modulus of b-arsenene and p-arsenene in armchair and zigzag directions. Each data point is averaged from 5 independent simulations and the error bars denote standard deviations.

system dimensions and eventually converge at around 100 nm^2. Therefore, moderate sized systems of 9.8 × 9.9 (x × y) nm^2 b-arsenene and 9.8 × 10.1 (x × y) nm^2 p-arsenene were selected in the following calculations to maintain good system stability and meanwhile save computational cost. It is worth noting that the system dimensions have negligible effects on Young's modulus, which indicates that the elastic deformations are insensitive to system sizes.

Next, we explore the effect of chirality on the mechanical properties of b-arsenene and p-arsenene. The system is uniaxially elongated at a strain rate of 1×10^{-4} ps^{-1} in the armchair x or zigzag y direction after it reaches the steady state at 100 K. The strain–stress profiles are shown in Fig. 3. It can be observed that the mechanical response is elastic at small strains with linear variations in the strain–stress curves. At higher strain levels, the strain–stress relations become non-linear and plastic deformations become dominant. The stress reaches its maximum value at the fracture point. The maximum stress that the system can withstand is defined as the fracture strength and the corresponding strain value is referred to as the fracture strain. The averaged fracture stain and strength for b-arsenene along the armchair and zigzag directions are 0.21, 7.4 GPa, and 0.24, 7.1 GPa, respectively. Compared to b-arsenene, p-arsenene possesses distinct fracture strains and strengths in the armchair (0.23 and 3.3 GPa) and zigzag (0.13 and 5.9 GPa) directions. For the puckered arsenene structure, the ultimate stresses along the zigzag direction are almost two times higher than those along the armchair direction, while the ultimate strains along the armchair direction are two times higher than those along the zigzag direction. This indicates that the strengths are higher in the zigzag direction while it is more brittle compared to the armchair direction. A similar phenomenon has also been observed in other puckered structures such as phosphorene.[40] This phenomenon has been confirmed by several DFT and MD calculations.[41–43] We further calculate the Young's moduli of b-arsenene and p-arsenene by fitting the strain–stress profiles for $\varepsilon < 0.02$. The calculated Young's moduli in the armchair and zigzag directions are 49.7 and 49.0 GPa for b-arsenene and 20.2 and 69.5 GPa for p-arsenene. The Young's modulus for b-arsenene agrees well with the DFT predicted result of 54.32 GPa by Akbari *et al.*[44] They also predicted the critical strain at 0.13 in the zigzag direction, which soundly matches the results of this work, which is 0.133 in the zigzag direction as shown in Fig. 3. Also using the first principles DFT method, Guo *et al.*[19] computed the fracture strain of the buckled arsenene at 0.2036, which also matches our calculated fracture strain of 0.20772. Based on the above results, it can be concluded that the MD simulation generated results in this work coincide well with those predicted by DFT methods and the method used in this work is well-justified. The mechanical property discrepancies between b-arsenene and p-arsenene can be attributed to their crystal structures. The fracture behaviors of the buckled and puckered structures are similar to those in α-phosphorene and β-phosphorene obtained by the ReaxFF potential.[45]

We further investigate the effects of temperature at different values 100, 200, 300, 400 and 500 K. The strain–stress profiles at different temperatures for b-arsenene are displayed in Fig. 4. Since the variation trends are similar, the strain–stress profiles of p-arsenene are not displayed separately. The fracture properties of b-arsenene deteriorate with increasing temperature in both chiral directions. The calculated fracture strain, fracture strength and Young's modulus are shown in Fig. 5. It can be observed that the mechanical properties of both b-arsenene and p-arsenene decrease monotonically with temperature. When the temperature increases from 100 to 500 K, the fracture strain and fracture strength for b-arsenene are reduced by 34.6% and 23.8% in the armchair direction and 41.7% and 23.2% in the zigzag direction. The Young's moduli are reduced by 5.9% and 5.7%, respectively. For p-arsenene, the fracture strain and fracture strength are reduced by 39.8% and 29.7% in the armchair direction and 50.5% and 37.8% in the zigzag direction. The Young's moduli are reduced by 8.3% and 5.3%. This temperature induced performance degradation resembles those of other 2D materials.[46–48] The temperature dependent strain–stress relations of phosphorene under

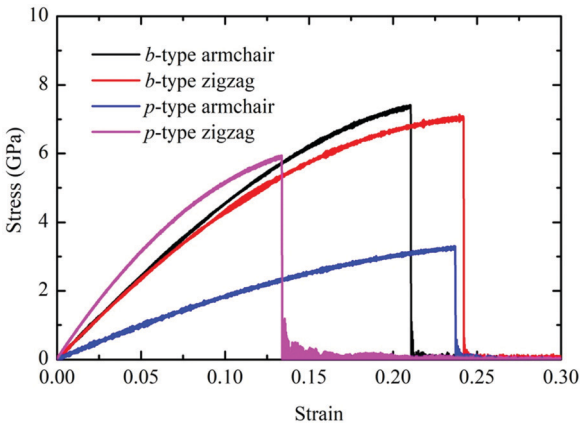

Fig. 3 Strain–stress profiles of b-arsenene and p-arsenene in armchair and zigzag directions.

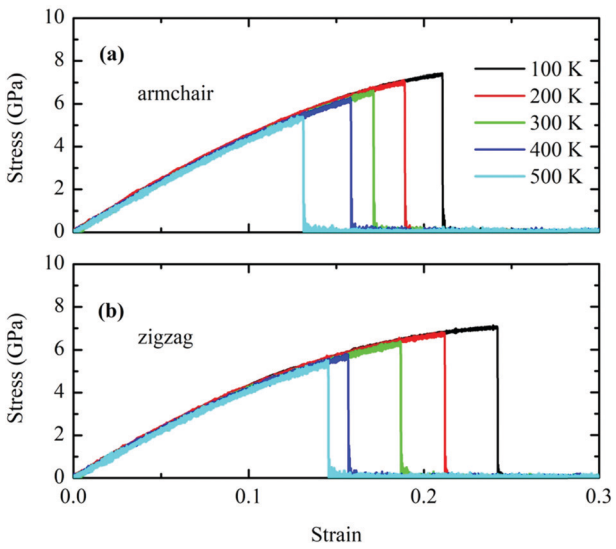

Fig. 4 Effects of temperature on the strain–stress profiles of b-arsenene in (a) armchair and (b) zigzag directions.

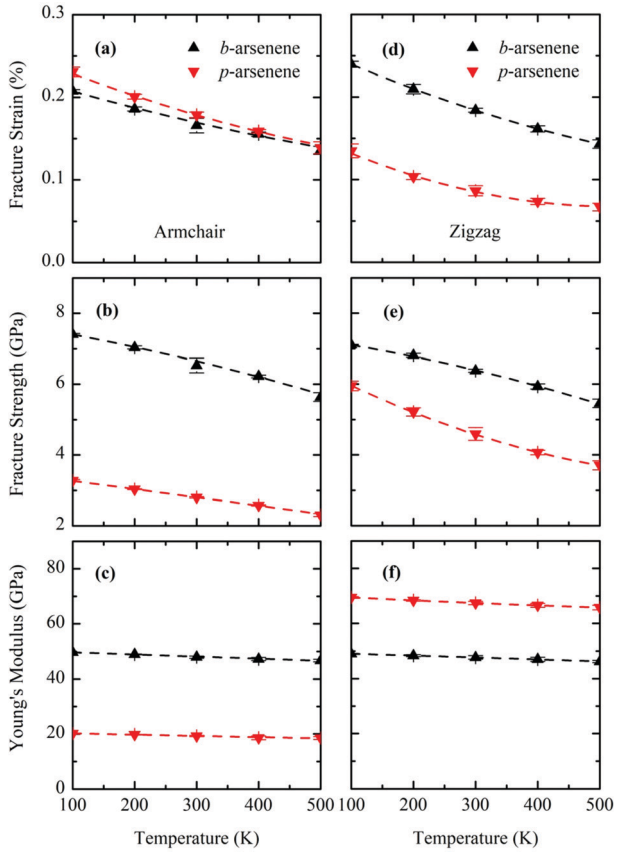

Fig. 5 Dependence of fracture strain, fracture strength and Young's modulus on temperature in (a)–(c) armchair direction and (d)–(f) zigzag direction.

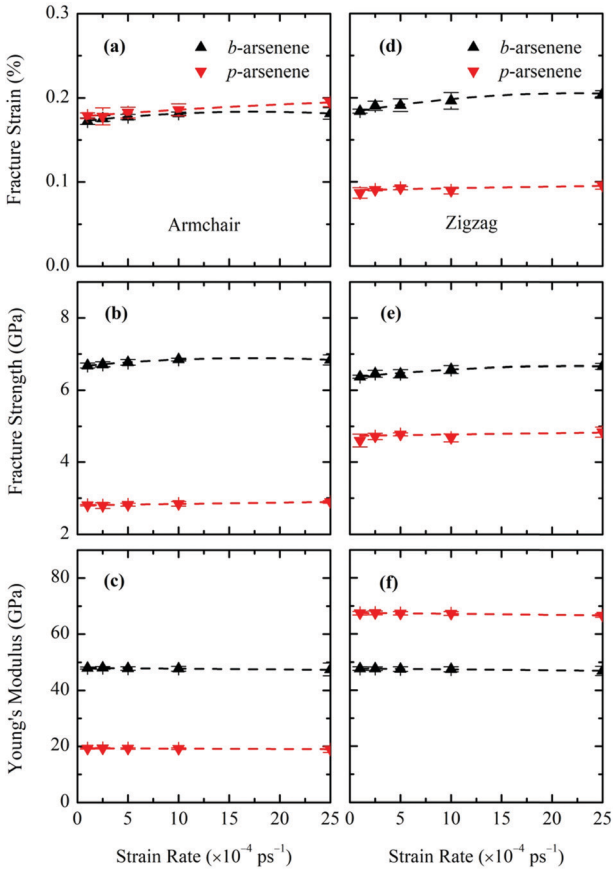

Fig. 6 Effects of strain rate on fracture strain, fracture strength and Young's modulus in (a)–(c) armchair direction and (d)–(f) zigzag direction.

uniaxial tension are investigated and similar results are obtained.[49,50] The effect of temperature can be explained by several factors. The increasing temperature enhances the atomic vibrations in the system, which weakens the covalent bonds in the crystal structure.[24,50,51] An extreme case is the structural collapsing of a material at its melting point. The binding energy among atoms decreases because of the applied tensile stress, which results in a lower energy barrier for chemical bond breakage. The rising temperature heightens the thermal fluctuations of atoms, which provides more probability to overcome the lower energy barrier.[19] Therefore, the higher temperature leads to the faster fracture formation and propagations in b-arsenene and p-arsenene. Aside from the aforementioned 1×10^{-4} ps^{-1} strain rate, another four strain rates of 2.5×10^{-4}, 5×10^{-4}, 1×10^{-3} and 2.5×10^{-3} ps^{-1} are also explored in this work. Fig. 6 shows the effect of strain rate on the fracture strains, fracture strengths and Young's moduli of b-arsenene and p-arsenene at 100 K. The increase of the strain rate has negligible effects on the mechanical properties of arsenene, which is in agreement with those of graphene and $MoSe_2$.[37]

The structural defects in 2D structures are particularly noticeable in chemically grown 2D materials due to the imperfection of the growth process.[52] Therefore, it is necessary to evaluate the mechanical properties of b-arsenene and p-arsenene at different defect ratios. There are multiple types of surface defect in monolayer structures, such as single-vacancy (SV), double-vacancy (DV), multi-vacancy (MV) and Stone–Wales (SW). Isotopic doping and surface functionalization are also considered as surface defects in many studies.[53–55] Even for the same amount of missing atoms, the thermal and mechanical properties of graphene could have distinct results depending on the type of defect.[56–59] To provide a better understanding of the larger representative volumes of defects on the mechanical properties, we created random defects containing SV, DV and MV with volume fractions of 0, 1, 2, 3, 4 and 5% in both b-arsenene and p-arsenene. To clearly demonstrate the fracture behavior differences in the armchair and zigzag directions, the crack propagations in single point vacancy defected b-arsenene and p-arsenene are shown in Fig. 7. A single vacancy system with a missing atom in the center is used to illustrate the crack formations and propagations. The contour colors represent the potential energy distributions. For both types of arsenenes, the structures in the zigzag direction are more brittle compared to those in the armchair direction, which is consistent with the strain–stress profiles shown in Fig. 3. The strain–stress profiles at different defect ratios are displayed in Fig. 8 for b-arsenene. Compared to the effects of temperature, the surface defect has stronger impacts on the mechanical properties of arsenene inducing sharp decreases of both fracture strains and strengths.

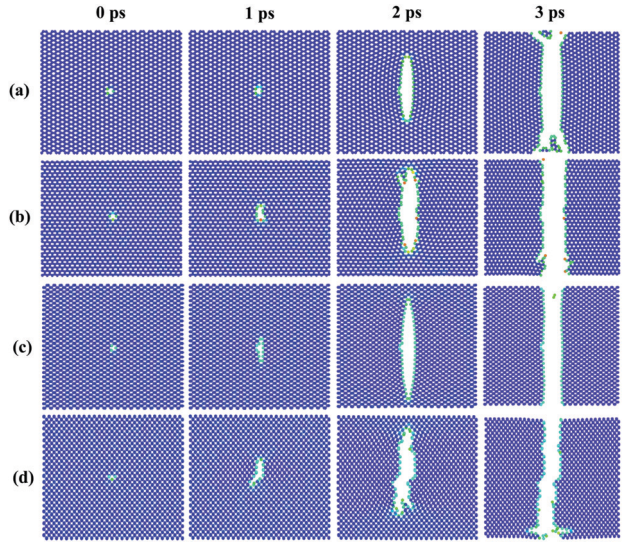

Fig. 7 Spatio-temporal crack propagations in single point defect (a) armchair b-arsenene, (b) zigzag b-arsenene, (c) armchair p-arsenene and (d) zigzag p-arsenene.

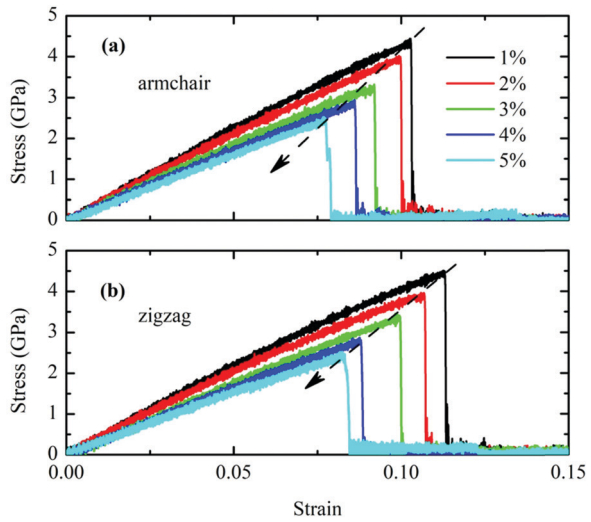

Fig. 8 Strain–stress profile variations with defect ratios from 1 to 5% in (a) armchair and (b) zigzag directions.

The results of the mechanical properties at different defect levels are shown in Fig. 9. When the random defect ratio increases from 0 to 5%, the fracture strain decreases by 79.3 and 85.7% for b-arsenene, and 80.8 and 78.4% for p-arsenene in the armchair and zigzag directions, respectively. The reductions of the corresponding fracture strength are 74.5 and 81.4% for b-arsenene, and 64.3 and 81.6% for p-arsenene. Similar results have been obtained in other 2D materials such as phosphorene. The effects of random defects on the failure behaviors of phosphorene were evaluated using MD simulations. With increasing defect ratios from 0 to 2%, the fracture strain dropped by 34% and 39% in the armchair and zigzag directions, respectively; the corresponding fracture strength decreased by 39% and 41%.[19] In another work by Nguyen *et al.*,[60] it was reported that due to defects,

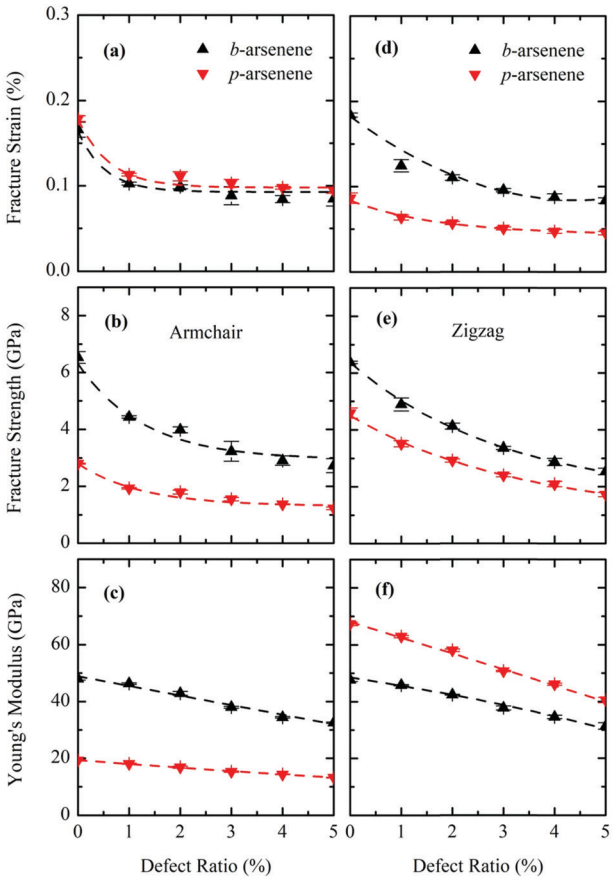

Fig. 9 Effects of defect on fracture strain, fracture strength and Young's modulus in (a)–(c) armchair direction and (d)–(f) zigzag direction.

the fracture strength and fracture strain of phosphorene can reduce up to 53% and 69%, respectively. Stress concentrations exist around the vacancy defect, which can influence the fracture behaviors.[61] Besides, the nucleation of fracture increases with the growing vacancy defect. The growing vacancy breaks the integrity of the pristine arsenene monolayer, which disrupts the covalent bonds and makes the material less stiff. Therefore, the crack forms and expands more rapidly during tensile stress.

4. Conclusion

In this work, the effects of system dimension, temperature, strain rate, and random surface defect on the critical fracture properties of buckled and puckered monolayer arsenenes are comprehensively explored. The fracture strain, fracture strength and Young's modulus are extracted from strain–stress profiles. It was discovered that the mechanical properties of b-arsenene are less anisotropic compared to those of p-arsenene. Similar to phosphorene, the strong anisotropic mechanical behaviors of p-arsenene originate from its distinct crystal structures in the armchair and zigzag directions. The mechanical properties of b-arsenene and p-arsenene deteriorate with temperature in both chiral directions. The fracture strain and fracture strength for b-arsenene are reduced by 34.6% and 23.8% in the armchair

direction and 41.7% and 23.2% in the zigzag direction when the temperature increases from 100 to 500 K. The Young's moduli are reduced by 5.9% and 5.7%, respectively. On the other hand, the mechanical properties of arsenene are less sensitive to the strain rate. The most significant impact factor on the mechanical properties of arsenene is surface defects. When the defect ratio increases from 0 to 5%, the fracture strain decreases by 79.3 and 85.7% for b-arsenene, and 80.8 and 78.4% for p-arsenene in the armchair and zigzag directions, respectively. The reductions of the corresponding fracture strength are 74.5 and 81.4% for b-arsenene, and 64.3 and 81.6% for p-arsenene. Our results provide fundamental knowledge on the mechanical properties of b-arsenene and p-arsenene.

Conflicts of interest

There are no conflicts of interest to declare.

Acknowledgements

The authors gratefully acknowledge the financial support from the Guangdong Province Science and Technology Project (no. 2017A040402005), the Guangzhou Bureau of Quality and Technical Supervision Science and Technology Project (no. 2017KJ19) and the National Natural Science Foundation of China (no. 51576145).

References

1 C. Lee, X. Wei, J. W. Kysar and J. Hone, *Science*, 2008, **321**, 385–388.
2 J. Zhang, X. Huang, Y. Yue, J. Wang and X. Wang, *Phys. Rev. B: Condens. Matter Mater. Phys.*, 2011, **84**, 235416.
3 Y. Yue, J. Zhang and X. Wang, *Small*, 2011, **7**, 3324–3333.
4 J. Zhang, Y. Wang and X. Wang, *Nanoscale*, 2013, **5**, 11598–11603.
5 J. Zhang and X. Wang, *Nanoscale*, 2013, **5**, 734–743.
6 J. Zhang, X. Wang and H. Xie, *Phys. Lett. A*, 2013, **377**, 721–726.
7 J. Zhao, Z. H. Qi, Y. Xu, J. Dai, X. C. Zeng, W. L. Guo and J. Ma, *WIREs Comput. Mol. Sci.*, 2019, **9**, e1387.
8 S. Sharma, S. Kumar and U. Schwingenschlogl, *Phys. Rev. Appl.*, 2017, **8**, 044013.
9 X. T. Sun, Y. X. Liu, Z. G. Song, Y. D. Li, W. Z. Wang, H. P. Lin, L. Wang and Y. Y. Li, *J. Mater. Chem. C*, 2017, **5**, 4159–4166.
10 H.-S. Tsai, S.-W. Wang, C.-H. Hsiao, C.-W. Chen, H. Ouyang, Y.-L. Chueh, H.-C. Kuo and J.-H. Liang, *Chem. Mater.*, 2016, **28**, 425–429.
11 G. Wang, R. Pandey and S. P. Karna, *ACS Appl. Mater. Interfaces*, 2015, **7**, 11490–11496.
12 S. Zhang, Z. Yan, Y. Li, Z. Chen and H. Zeng, *Angew. Chem., Int. Ed.*, 2015, **54**, 3112–3115.
13 C. Kamal and M. Ezawa, *Phys. Rev. B: Condens. Matter Mater. Phys.*, 2015, **91**, 085423.
14 C. Wang, Q. Xia, Y. Nie, M. Rahman and G. Guo, *AIP Adv.*, 2016, **6**, 035204.
15 Z. F. Xie, F. W. Sun, R. Yao, Y. Zhang, Y. H. Zhang, Z. H. Zhang, J. B. Fan, L. Ni and L. Duan, *Appl. Surf. Sci.*, 2019, **475**, 839–846.
16 H. J. Zhang, Y. D. Ma and Z. F. Chen, *Nanoscale*, 2015, **7**, 19152–19159.
17 Y. P. Wang, C. W. Zhang, W. X. Ji, R. W. Zhang, P. Li, P. J. Wang, M. J. Ren, X. L. Chen and M. Yuan, *J. Phys. D: Appl. Phys.*, 2016, **49**, 055305.
18 W. Q. Xu, P. F. Lu, L. Y. Wu, C. H. Yang, Y. X. Song, P. F. Guan, L. H. Han and S. M. Wang, *IEEE J. Sel. Top. Quantum Electron.*, 2017, **23**, 9000305.
19 D. Guo, B. Shao, C. Li and Y. Ma, *Superlattices Microstruct.*, 2016, **100**, 324–334.
20 S. L. Zhang, Z. Yan, Y. F. Li, Z. F. Chen and H. B. Zeng, *Angew. Chem., Int. Ed.*, 2015, **54**, 3112–3115.
21 G. Pizzi, M. Gibertini, E. Dib, N. Marzari, G. Iannaccone and G. Fiori, *Nat. Commun.*, 2016, **7**, 12585.
22 A. Taheri, C. Da Silva and C. H. Amon, *Phys. Chem. Chem. Phys.*, 2018, **20**, 27611–27620.
23 B. F. Zhang, H. Zhang, J. H. Lin and X. L. Cheng, *Phys. Chem. Chem. Phys.*, 2018, **20**, 30257–30266.
24 M. Q. Chen, S. S. Quek, Z. D. Sha, C. H. Chiu, Q. X. Pei and Y. W. Zhang, *Carbon*, 2015, **85**, 135–146.
25 S. Shadlou, B. Ahmadi-Moghadam and F. Taheri, *Mater. Des.*, 2014, **59**, 439–447.
26 L. J. Yi, Z. N. Yin, Y. Y. Zhang and T. C. Chang, *Carbon*, 2013, **51**, 373–380.
27 H. Zhao and N. R. Aluru, *J. Appl. Phys.*, 2010, **108**, 064321.
28 Q. X. Pei, Z. D. Sha, Y. Y. Zhang and Y. W. Zhang, *J. Appl. Phys.*, 2014, **115**, 023519.
29 T. W. Han, Y. Luo and C. Y. Wang, *J. Phys. D: Appl. Phys.*, 2014, **47**, 025303.
30 Y. Chen, H. Xiao, Y. L. Liu and X. Chen, *J. Phys. Chem. C*, 2018, **122**, 6368–6378.
31 L. Y. Zhu, T. T. Zhang, Z. M. Sun, J. H. Li, G. B. Chen and S. Y. A. Yang, *Nanotechnology*, 2015, **26**, 465707.
32 J. W. Jiang, *Sci. Rep.*, 2015, **5**, 7814.
33 C. Wei, K. Cho and D. Srivastava, *Phys. Rev. B: Condens. Matter Mater. Phys.*, 2003, **67**, 115407.
34 S. Plimpton, *J. Comput. Phys.*, 1995, **117**, 1–19.
35 J.-W. Jiang and Y.-P. Zhou, *Parameterization of Stillinger-Weber Potential for Two-Dimensional Atomic Crystals*, Intechopen, 2017, DOI: 10.5772/intechopen.71929.
36 F. Gong, Z. Ding, Y. Fang, C.-J. Tong, D. Xia, Y. Lv, B. Wang, D. V. Papavassiliou, J. Liao and M. Wu, *ACS Appl. Mater. Interfaces*, 2018, **10**, 14614–14621.
37 X. Wang, Y. Hong, M. Wang, G. Xin, Y. Yue and J. Zhang, *Phys. Chem. Chem. Phys.*, 2019, **21**, 9159–9167.
38 S. Susarla, P. Manimunda, Y. Morais Jaques, J. A. Hachtel, J. C. Idrobo, S. A. Syed Amnulla, D. S. Galvão, C. S. Tiwary and P. M. Ajayan, *ACS Nano*, 2018, **12**, 4036–4044.
39 T. Liang, P. Zhang, P. Yuan, S. Zhai and D. Yang, *Nano Futures*, 2019, **3**, 015001.
40 Z. Yang, J. Zhao and N. Wei, *Appl. Phys. Lett.*, 2015, **107**, 023107.
41 A. Maryam, G. Abbas, M. Rashid and A. Sattar, *Chin. Phys. B*, 2018, **27**, 017401.
42 L. L. Li and J. Yang, *Nanotechnology*, 2017, **28**, 475701.
43 J. W. Jiang and H. S. Park, *J. Phys. D: Appl. Phys.*, 2014, **47**, 385304.

44 O. Akbari, R. Ansari and S. Rouhi, *Mater. Res. Express*, 2018, **5**, 015025.
45 M.-Q. Le, *Nanotechnology*, 2018, **29**, 195701.
46 D. K. Das, J. Sarkar and S. K. Singh, *Comput. Mater. Sci.*, 2018, **151**, 196–203.
47 F. Memarian, A. Fereidoon, S. Khodaei, A. H. Mashhadzadeh and M. D. Ganji, *Vacuum*, 2017, **139**, 93–100.
48 F. Lin, Y. Xiang and H. S. Shen, *Composites, Part B*, 2017, **111**, 261–269.
49 Z. D. Sha, Q. X. Pei, Z. W. Ding, J. W. Jiang and Y. W. Zhang, *J. Phys. D: Appl. Phys.*, 2015, **48**, 395303.
50 Z. Y. Yang, J. H. Zhao and N. Wei, *Appl. Phys. Lett.*, 2015, **107**, 023107.
51 J. H. Zhao, J. W. Jiang and T. Rabczuk, *Appl. Phys. Lett.*, 2013, **103**, 231913.
52 W. Zhou, X. Zou, S. Najmaei, Z. Liu, Y. Shi, J. Kong, J. Lou, P. M. Ajayan, B. I. Yakobson and J.-C. Idrobo, *Nano Lett.*, 2013, **13**, 2615–2622.
53 K. C. Katakam, P. Gupta and N. Yedla, *J. Mater. Eng. Perform.*, 2019, **28**, 63–78.
54 J. Gruber, X. W. Zhou, R. E. Jones, S. R. Lee and G. J. Tucker, *J. Appl. Phys.*, 2017, **121**, 195301.
55 H. N. Wu, D. S. Xu, H. Wang and R. Yang, *J. Mater. Sci. Technol.*, 2016, **32**, 1033–1042.
56 K. Chu, J. Wang, Y. P. Liu and Z. R. Geng, *Carbon*, 2018, **140**, 112–123.
57 K. Kim, K. H. Nam, J. Lee, H. J. Kim, M. Goh, B. C. Ku and N. H. You, *Carbon*, 2017, **122**, 614–621.
58 Y. F. Gao, Y. H. Jing, J. Q. Liu, X. C. Li and Q. Y. Meng, *Appl. Therm. Eng.*, 2017, **113**, 1419–1425.
59 S. H. Tan, L. M. Tang, Z. X. Xie, C. N. Pan and K. Q. Chen, *Carbon*, 2013, **65**, 181–186.
60 D.-T. Nguyen, M.-Q. Le, V.-T. Nguyen and T.-L. Bui, *Superlattices Microstruct.*, 2017, **112**, 186–199.
61 A. H. N. Shirazi, R. Abadi, M. Izadifar, N. Alajlan and T. Rabczuk, *Comput. Mater. Sci.*, 2018, **147**, 316–321.